JACS
JOURNAL OF THE AMERICAN CHEMICAL SOCIETY

Article

pubs.acs.org/JACS

The Formation Mechanism of Fluorescent Metal Complexes at the $Li_xNi_{0.5}Mn_{1.5}O_{4-\delta}$/Carbonate Ester Electrolyte Interface

Angélique Jarry,[†] Sébastien Gottis,[†] Young-Sang Yu,[‡,§] Josep Roque-Rosell,[‡] Chunjoong Kim,[§] Jordi Cabana,[§] John Kerr,[†] and Robert Kostecki*[,†]

[†]Environmental Energy Technologies Division, Lawrence Berkeley National Laboratory, Berkeley, California 94720, United States
[‡]Advanced Light Source, Lawrence Berkeley National Laboratory, Berkeley, California 94720, United States
[§]Department of Chemistry, University of Illinois at Chicago, 845 West Taylor Street, Chicago, Illinois 60607, United States

Supporting Information

ABSTRACT: Electrochemical oxidation of carbonate esters at the $Li_xNi_{0.5}Mn_{1.5}O_{4-\delta}$/electrolyte interface results in Ni/Mn dissolution and surface film formation, which negatively affect the electrochemical performance of Li-ion batteries. Ex situ X-ray absorption (XRF/XANES), Raman, and fluorescence spectroscopy, along with imaging of $Li_xNi_{0.5}Mn_{1.5}O_{4-\delta}$ positive and graphite negative electrodes from tested Li-ion batteries, reveal the formation of a variety of $Mn^{II/III}$ and Ni^{II} complexes with β-diketonate ligands. These metal complexes, which are generated upon anodic oxidation of ethyl and diethyl carbonates at $Li_xNi_{0.5}Mn_{1.5}O_{4-\delta}$, form a surface film that partially dissolves in the electrolyte. The dissolved Mn^{III} complexes are reduced to their Mn^{II} analogues, which are incorporated into the solid electrolyte interphase surface layer at the graphite negative electrode. This work elucidates possible reaction pathways and evaluates their implications for Li^+ transport kinetics in Li-ion batteries.

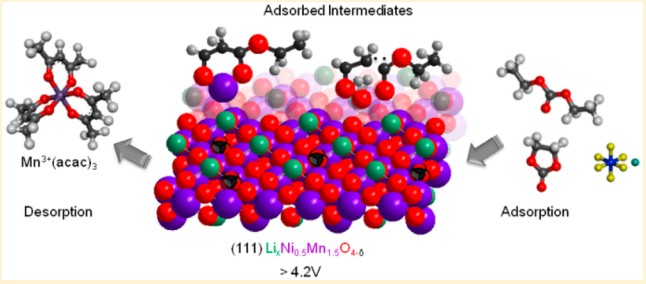

INTRODUCTION

A basic understanding of the mechanism of interfacial interactions between electrodes and organic electrolytes in electrochemical systems is a critical requirement for developing substantial improvements to electrical energy storage (EES) devices. The lithium-ion battery is an example of a ubiquitous EES system that is inherently unstable and relies on the formation of protective surface films at the surface of electrode(s). $LiNi_{0.5}Mn_{1.5}O_4$ spinel, which is a promising Li-ion positive electrode material for high-energy-density Li-ion systems, operates at high potential (ca. 4.8 V vs Li/Li^+), which is above the thermodynamic stability window of standard organic-carbonate-based electrolytes.[1] The surface chemical reactivity of $LiNi_{0.5}Mn_{1.5}O_{4-\delta}$ in Li-ion batteries results in electrolyte oxidation that yields diverse products such as carbon dioxide, aldehydes, alcohols, hydrogen fluoride, lithium ethoxide, oxygen, hydrogen, and transesterification products.[2−5]

These compounds contribute to the formation of surface protective films that extend battery life.[6−8] On the other hand, the electrolyte oxidation is accompanied by gradual Ni/Mn dissolution, up to 2 atom %, which leads to severe loss of electrochemical performance of the graphite negative electrode and the entire Li-ion cell.[6] The mechanism and kinetics of interfacial reactions, along with the corresponding chemical composition and structure of the electrode and electrolyte, are still not well understood.[2,5,9,10] It is commonly accepted that the mechanism for Mn and Ni dissolution involves a disproportionation reaction of Mn^{III} to Mn^{II} and Mn^{IV}.[11] It is also assumed that free Mn^{2+} ions move toward the negative electrode, where they are reduced to metallic Mn.[6] However, recent reports indicate the presence of Mn^{II} and Ni^{II} on the surface of graphite negative electrodes.[12,13] Shkrob et al. have suggested that Mn^{II} species are manganese acetate.[14] Zhan et al.[12] demonstrated that the impedance of the graphite anode is directly proportional to the concentration of Mn^{II} species in the solid electrolyte interphase (SEI) layer. There is no doubt that Mn^{II} species originate from the Mn-based oxide positive electrode. However, their exact nature, composition, mechanism of formation, and interactions with the SEI layer on the negative electrode remain largely unknown.

$LiNi_{0.5}Mn_{1.5}O_4$ crystallizes in a spinel structure with Ni/Mn and Li in octahedral and tetrahedral environments of oxygen atoms, respectively (Figure 1).[1,2,7,15−17] The reactivity of $LiNi_{0.5}Mn_{1.5}O_4$ spinel toward the electrolyte strongly depends on the surface crystalline orientation, local defects, and surface reconstruction processes.[15−21] For example, the (111) facet is the most prevalent surface orientation of $LiNi_{0.5}Mn_{1.5}O_{4-\delta}$ microparticles and allows fast lithiation/delithiation kinetics.[15−17] Surface oxygen vacancies, which are preferentially located in Ni-rich and Mn-depleted regions, modify the local surface charge density distribution.[18−21] The activation energy

Received: November 23, 2014
Published: February 25, 2015

DOI: 10.1021/ja5116698
J. Am. Chem. Soc. 2015, 137, 3533−3539

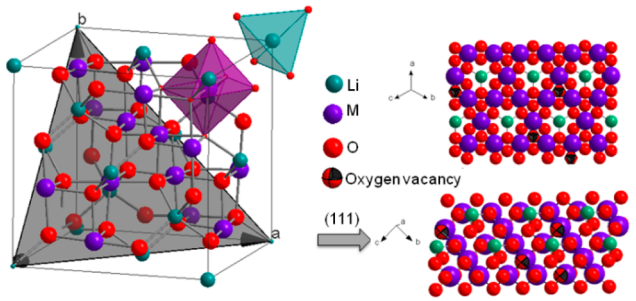

Figure 1. Schematic representation of the $LiNi_{0.5}Mn_{1.5}O_{4-\delta}$ (111) surface structure.

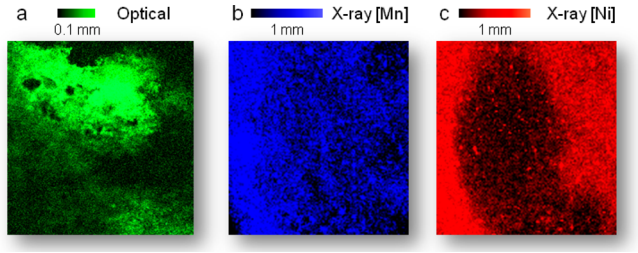

Figure 2. Optical and X-ray fluorescence images of the graphite negative electrode from a tested Li-ion cell. (a) Optical fluorescence image (488 nm excitation). (b, c) XRF maps of the (b) Mn and (c) Ni elemental distributions (λ_{ex} = 8500 eV).

of lithium deintercalation and the strength of Mn−O and Ni−O bonds are significantly lower adjacent to those oxygen vacancies, which are flanked by coordinately unsaturated Mn^{III} sites.[16,20] These peculiar surface properties of transition-metal oxides play a major role in heterogeneous catalytic processes,[22] such as oxidation of organic solvents, which are almost always associated with transition-metal reduction and dissolution.[23]

Although numerous attempts have been made to elucidate the nature of these interfacial phenomena in EES systems,[3,9,10,24−26] uncertainties due to the complex interrelated chemical and electrochemical phenomena and inherent limitations of the analytical techniques still remain.[27] Interestingly, post-mortem diagnostic evaluations of aged commercial and model Li-ion cells reveal strong and omnipresent fluorescence from electrodes and passive cell components.[28,29] In fact, the fluorescent emission from electrolyte decomposition products in Li-ion cathodes constitutes a major obstacle for in situ Raman probing of electrochemical interfaces in Li-ion systems.[30] Recent Raman measurements on a $LiNi_{0.5}Mn_{1.5}O_{4-\delta}$ electrode in a 1 M $LiPF_6$ ethylene carbonate (EC):diethyl carbonate (DEC) (1:2 w/w) electrolyte revealed that the formation of fluorescent compounds at potentials above 4.2 V coincides with the threshold of $Mn^{III} \rightarrow Mn^{IV}$ and $Ni^{II} \rightarrow Ni^{IV}$ oxidation and Li^+ removal from the $LiNi_{0.5}Mn_{1.5}O_{4-\delta}$ host lattice.[24,29] Interestingly, these processes also overlap with manganese and nickel dissolution,[31] which suggests that the fluorescent compounds could be metal-ion-based.[29] Consequently, the fluorescence effect in Li-ion systems can offer a unique insight into interfacial phenomena, including the mechanism of Ni/Mn dissolution, especially when combined with other spectroscopic and imaging techniques such as X-ray absorption.[32−35] This study provides a detailed description of possible reaction pathways leading to the formation of fluorescent metal complexes at the $Li_xNi_{0.5}Mn_{1.5}O_{4-\delta}$ surface in organic carbonate electrolytes.

RESULTS AND DISCUSSION

Figure 2 shows an ex situ optical fluorescence image and X-ray fluorescence (XRF) distribution maps of Ni and Mn on the graphite negative electrode from a tested $Li_xNi_{0.5}Mn_{1.5}O_{4-\delta}$/graphite/1 M $LiPF_6$ EC:DEC (1:2 w/w) coin cell that was cycled 600 times (see Figure 1 in the Supporting Information). The shades of green in the optical fluorescence image represent the relative signal intensity integrated between 505 and 645 nm upon excitation at 488 nm (Figure 2a). The cycled graphite electrode exhibits a nonuniform fluorescence emission pattern from electrolyte decomposition compounds on the electrode's surface. Interestingly, XRF images of the cycled graphite electrode (Figure 2b,c) reveal irregular Ni and Mn distribution patterns somewhat similar to the optical fluorescence images. The observed segregation in the Ni and Mn elemental maps indicates the presence of Ni/Mn species with different chemical affinities for chemical compounds in the SEI layer. The close similarity of the optical and X-ray fluorescence patterns suggests a possible correlation between the observed optical fluorescence emission and the presence of Mn and Ni, which originated from the $Li_xNi_{0.5}Mn_{1.5}O_{4-\delta}$ positive electrode.

The number of metal-ion-based fluorochromes that can form upon oxidation of carbonate-ester-based electrolytes at the $Li_xNi_{0.5}Mn_{1.5}O_{4-\delta}$ surface is very limited. Oxidation of carbonate esters can produce a variety of products, including carbon dioxide, oxalates, and carbonates.[4] However, Ni and Mn oxalates and carbonates display very weak or no fluorescence. Fluorescent calcites (ACO_3, A = Ca, Mg, Zn) with Mn^{II} activators are excluded as possible candidates by the absence of alkaline-earth metals in the system. A possible source of fluorescence is distorted octahedral complexes with transition-metal centers and weak-field ligands, which are known to be strong fluorescence emitters because of their multiple metal d−d or metal-to-ligand charge transfer (MLCT) electronic transitions in the 450−650 nm range. In such complexes, the strongest coupling is observed from the fivefold-degenerate 3d metal orbitals, which are split into at least two different energy levels (e_g and t_{2g}). Additional splitting of energy levels due to Jahn−Teller distortion and spin−orbit interactions also occurs, allowing weak, spin-forbidden electronic transitions. These multiple electronic energy levels may become accessible upon a single-wavelength excitation and give rise to broad fluorescence emission similar to the spectra observed in the cycled/aged Li-ion cell (Figure 2a).

Transition-metal acetylacetonate (acac) complexes constitute a class of such fluorescent complexes, which are likely the source of fluorescence in Li-ion systems. In fact, the peculiar properties of distorted octahedral Ni^{II}, Mn^{II}, and Mn^{III} acac complexes have been extensively studied for many decades.[36−39] The trimeric Ni^{II} bis(acetylacetonate), Mn^{II} bis(acetylacetonate), and Mn^{III} tris(acacetylacetonate) complexes display strong geometric distortions along the *x*, *y*, and *z* axes, respectively, leading to splitting of the originally fivefold-degenerate 3d orbitals into five distinct levels. The multiple d−d electronic transitions, accessible with a single-wavelength excitation, are predicted at wavelengths of ca. 500 nm for these manganese complexes.[37] The fluorescence emissions from Mn^{II} bis(acetylacetonate) and Ni^{II} bis(acetylacetonate) are weaker than that from Mn^{III} tris(acetylacetonate) because the d−d transition is spin-forbidden and the d−d transition at 650 nm has low quantum yield, respectively.[40] Importantly for this

DOI: 10.1021/ja5116698
J. Am. Chem. Soc. 2015, 137, 3533−3539

investigation of Li-ion systems, those metal complexes are stable and soluble in carbonate ester solvents.

To confirm the origin and nature of fluorescent species in Li-ion cells, we employed a multitude of characterization methods, including optical and X-ray-based techniques. Unfortunately, probing functional electrochemical interfaces in Li-ion systems with standard in situ and ex situ techniques produces results that are invariably convoluted, often defying accurate interpretation solely on the basis of the measured fingerprints. A perplexing example of such elusive phenomena is a dissolution process of Mn and Ni from LiMNO electrode materials in Li-ion batteries.

Disappointingly, Fourier transform infrared spectroscopy (FTIR) and X-ray photoelectron spectroscopy (XPS) measurements produced results that were either inconclusive or meaningless (not shown here). To mitigate inherent shortcomings of FTIR,[3] we introduced fluorescence spectroscopy and imaging as a valuable new class of characterization tools for elucidating the function and operation of electrode materials. On the other hand, XRF and X-ray absorption near-edge structure (XANES) proved in this case to be far more effective in terms of sensitivity, selectivity, and specificity than XPS.

Ex situ Raman and X-ray absorption spectroscopy measurements were carried out on the cycled $Li_xNi_{0.5}Mn_{1.5}O_{4-\delta}$ positive and graphite negative electrodes. Spectra of selected reference compounds (i.e., trimeric Mn^{III} tris(acetylacetonate), Mn^{II}/Ni^{II} bis(acetylacetonate), and Ni/Mn carbonates and oxalates) were also recorded (Figure 3). The Raman spectra of the cycled $Li_xNi_{0.5}Mn_{1.5}O_{4-\delta}$ and graphite electrodes display characteristic broad fluorescence background profiles. The strong fluorescence emission obscures the Raman scattering signals from the $Li_xNi_{0.5}Mn_{1.5}O_{4-\delta}$ and graphite. Remarkably, the fluorescence background profile from the cycled $Li_xNi_{0.5}Mn_{1.5}O_{4-\delta}$ positive electrode appears very similar to that of Mn^{III} tris(acetylacetonate), whereas the spectrum of the cell separator and graphite negative electrode resembles that of Mn^{II} bis(acetylacetonate). This indicates that Mn^{III} tris(acetylacetonate), which forms at the positive electrode, partially dissolves in the electrolyte and is then reduced to Mn^{II} bis(acetylacetonate) upon reaction with the solvents and/or negative electrode. In addition, the strong fluorescence emission from Mn^{III} tris(acetylacetonate) may obscure weaker fluorescence signals from other optically active compounds that may also be present in the cell (i.e., Mn^{II}/Ni^{II} bis(acetylacetonate), Mn/Ni carbonates, and Mn/Ni oxalates).

The normalized Mn and Ni K-edge XANES spectra of the cycled graphite electrode (Figure 3c,d) exhibit spectral features of Mn^{II}/Ni^{II} bis(acetylacetonate), Ni/Mn carbonates, and oxalates. A linear combination of Mn^{II} bis(acetylacetonate) (67 ± 5%) and Mn^{II} oxalate (33 ± 5%) reference spectra produced an excellent fit to the experimental Mn K-edge XANES spectrum of the graphite negative electrode (Figure 3e; also see Table 1 in the Supporting Information). On the other hand, superposition of nickel carbonate (72 ± 5%) and Ni^{II} bis(acetylacetonate) (28 ± 5%) reference spectra yielded the Ni K-edge XANES spectrum (Figure 3f; also see Table 1 in the Supporting Information). These results confirm that Ni^{II} and Mn^{II} are the dominant valence states at the surface of the negative electrode and that β-diketonate ligands, carbonate, and oxalate anions are present in their immediate molecular environment. In fact, the presence of such distorted octahedral Mn and/or Ni complexes with β-diketonate ligands is the only

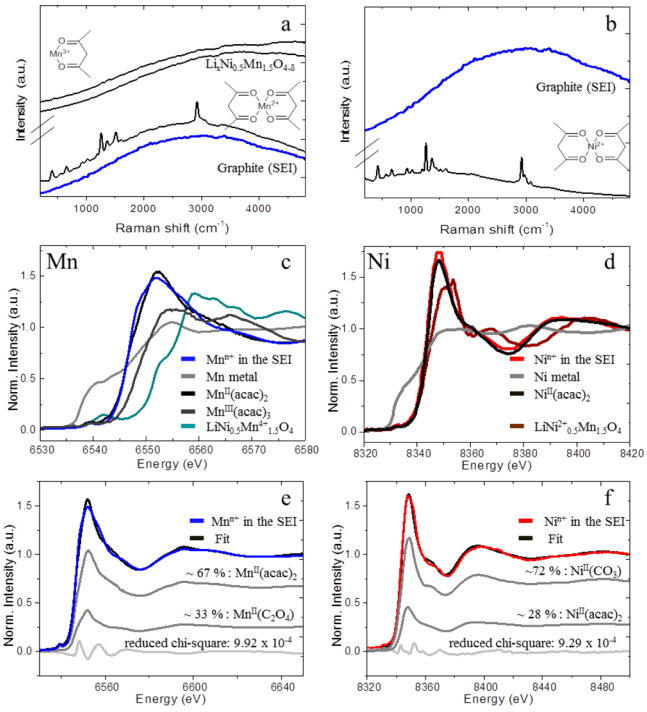

Figure 3. Identification of the manganese and nickel species at the positive and negative electrodes. (a, b) Ex situ Raman spectra of the cycled $LiNi_{0.5}Mn_{1.5}O_{4-\delta}$ positive and graphite negative electrodes, Mn^{III} tris(acetylacetonate), trimeric Mn^{II} bis(acetylacetonate), and trimeric Ni^{II} bis(acetylacetonate). (c, d) Normalized Mn and Ni K-edge XANES spectra of the cycled graphite electrode, Ni and Mn metal foils, Mn^{III} tris(acetylacetonate), Mn^{II}/Ni^{II} bis(acetylacetonate), and $LiNi_{0.5}Mn_{1.5}O_{4-\delta}$. (e, f) Linear combination fit results of XANES spectra from the cycled graphite electrode with Mn^{II} bis(acetylacetonate), Mn^{III} tris(acetylacetonate), Ni^{II} bis(acetylacetonate), Mn^{II}/Ni^{II} oxalate, and Mn^{II}/Ni^{II} carbonate as references.

plausible explanation of the observed optical fluorescence and the XANES spectral features.

Variations in the distributions of Mn and Ni compounds are directly linked with the electrochemical reactivities of Mn and Ni surface sites in $Li_xNi_{0.5}Mn_{1.5}O_{4-\delta}$. Density functional theory calculations by Sushko et al.[20] showed that surface oxygen vacancies redistribute local charge density in $Li_xNi_{0.5}Mn_{1.5}O_{4-\delta}$. Oxygen vacancies are preferentially surrounded by Ni^{II} and Mn^{III} with highly occupied Mn^{III} e_g energy levels, resulting in a lower oxidation potential. Therefore, early stages of Li^+ deintercalation at potentials below 4.7 V preferentially occur in the vicinity of oxygen vacancies and are coupled with Mn^{III} oxidation to Mn^{IV} [20] rather than Ni^{II} oxidation to Ni^{IV}, which dominates at higher potentials of ~4.8 V.

First-principles calculations also indicate that carbonate ester solvents can be oxidized via electron and proton transfer independent of the chemical composition of the electrode surface.[41,42] Linear carbonates are more easily oxidized than cyclic carbonates, and their oxidation potential is further lowered in the presence of PF_6^- anions.[41] The calculated oxidation potential of 4.5 V for dimethyl carbonate (DMC)/PF_6^- is 1.2 V lower than the theoretical value for isolated DMC. Interactions between the solvents and oxide lattice oxygens further lower the DMC oxidation potential to 4.2 V.[42]

The mechanism of EC oxidation at the (111) surface of $Li_xMn_2O_4$ ($x \geq 0.67$) proposed by Kumar et al.[42] involves a two-electron transfer associated with single deprotonation of

DOI: 10.1021/ja5116698
J. Am. Chem. Soc. 2015, 137, 3533−3539

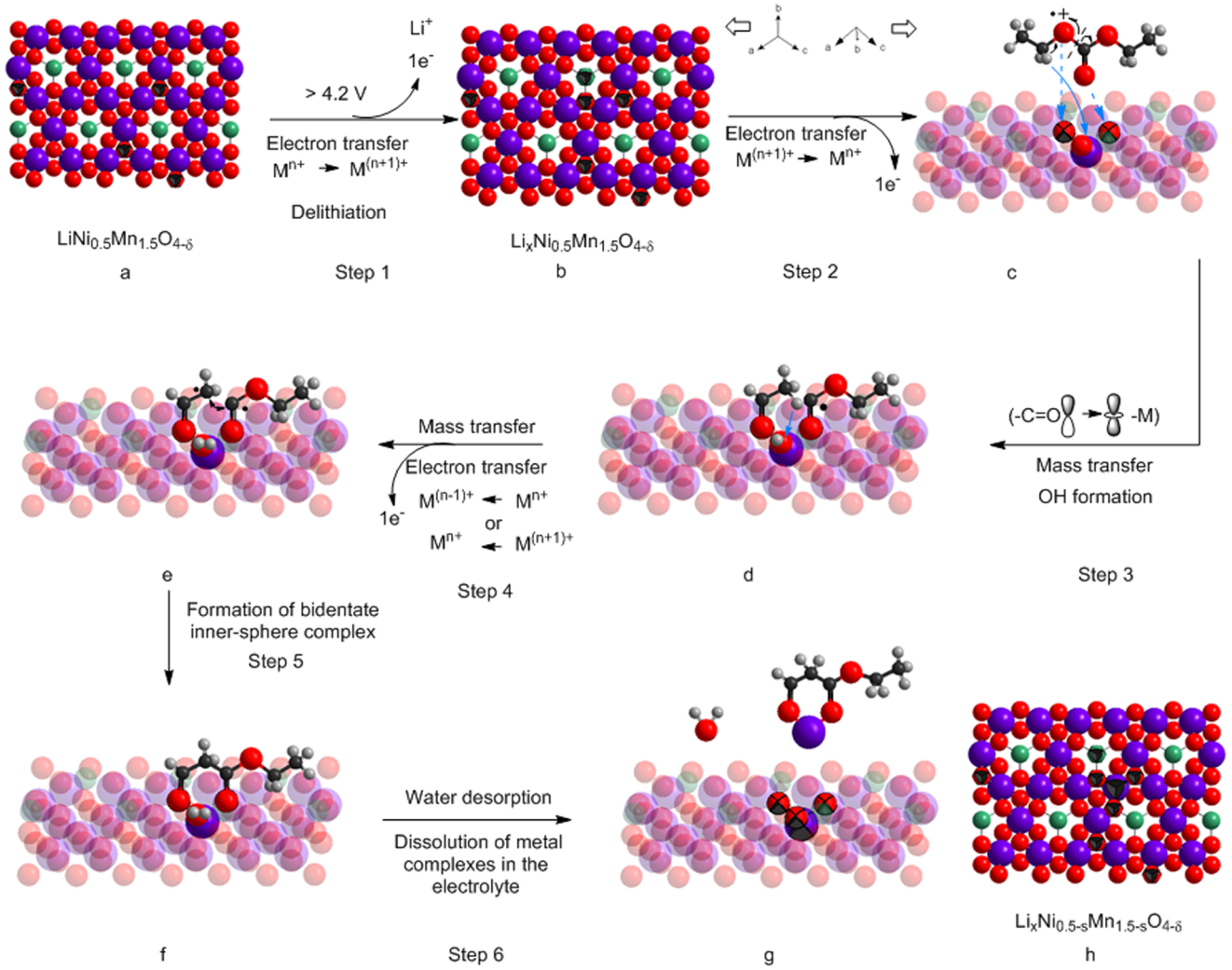

Figure 4. Possible formation pathway of the metal complexes upon DEC oxidation at the $Li_xNi_{0.5}Mn_{1.5}O_4$ surface by two proton-coupled electron transfer (PCET) processes associated with ligand adsorption. (a) Top view of the $LiNi_{0.5}Mn_{1.5}O_{4-\delta}$ (111) structure before cycling. Step 1: Delithiation accompanied by an oxidation of a transition metal (preferentially $Mn^{III} \rightarrow Mn^{IV}$) in the vicinity of an oxygen vacancy and possible creation of an oxygen vacancy (b). Steps 2−4: Two all-concerted PCET pathways with ligand adsorption. Step 2 is initiation of the cation radical at potentials >4.2 V accompanied by an electron transfer inducing a metal ion reduction (preferentially $Mn^{IV} \rightarrow Mn^{III}$) (c). Step 3 is adsorption of carbonate radical on the $Li_xNi_{0.5}Mn_{1.5}O_{4-\delta}$ surface accompanied by a heterolytic C−H bond cleavage, resulting in OH^- surface formation and adsorption of acetaldehyde on the adjacent oxygen sites (d). Step 4 is the second PCET, in which the C−H bond interacts with OH surface species, leading to the formation of adsorbed water, the formation of a second radical, and an electron transfer to a surficial metal (preferentially $Mn^{IV} \rightarrow Mn^{III}$) (e). Step 5: Radical termination reaction resulting in C−C bond formation and corresponding adsorbed complexes (f). Step 6: Desorption of water and of a bidentate complex (g). (h) $Li_xNi_{0.5}Mn_{1.5}O_{4-\delta}$ (111) structure after partial delithiation.

the EC ethyl group. A proton-coupled electron transfer (PCET) leads to the formation of hydroxyl surface species and the EC ring-opening reaction (C−O bond cleavage accompanied by the second electron transfer), which yields organic radicals chemisorbed at Li surface sites on $Li_xMn_2O_4$. All of these reactions are sensitive to the electrode potential, surface crystalline orientation, and surface concentrations of lithium and oxygen vacancies.[42] This study also indicates that the concentration of surface oxygen vacancies increases during the delithiation process.[20,42]

Molecular electrochemists have also extensively studied environemental chemical processes such as adsorption of ligands on mineral surfaces.[23,26,43,44] Duckworth and Martin[43] demonstrated that the rate of transition-metal dissolution during catalytic oxidation of organic solvents at transition-metal oxides is accelerated by a combination of proton adsorption and ligand adsorption associated with metal reduction in an acidic environment. Therefore, in the following proposed mechanisms, PCET pathways inducing a supplement of driving force for oxidation,[26,44] and in particular for all-concerted mechanisms (PCET with ligand adsorptions), are favored.

The postulated reaction pathways that lead to the formation of the observed Ni/Mn complexes with β-diketonate chelate ligands during oxidation of DEC and EC at the $Li_xNi_{0.5}Mn_{1.5}O_4$ surface are depicted in Figures 4 and 5, respectively. DEC oxidation at the $LiNi_{0.5}Mn_{1.5}O_{4-\delta}$ surface involves all-concerted mechanisms with two PCET processes that conclude with the formation of adsorbed β-diketonate ligands (Figure 4). Upon initial delithiation of $LiNi_{0.5}Mn_{1.5}O_{4-\delta}$ at potentials higher than 4.2 V, Mn^{III} atoms near oxygen vacancies are preferentially oxidized to Mn^{IV}.[20] Vacant d orbitals of those surficial Mn^{IV} atoms can easily overlap with an orbital of the carbonyl group in the DEC molecule to form coordination bonds.

DOI: 10.1021/ja5116698
J. Am. Chem. Soc. 2015, 137, 3533−3539

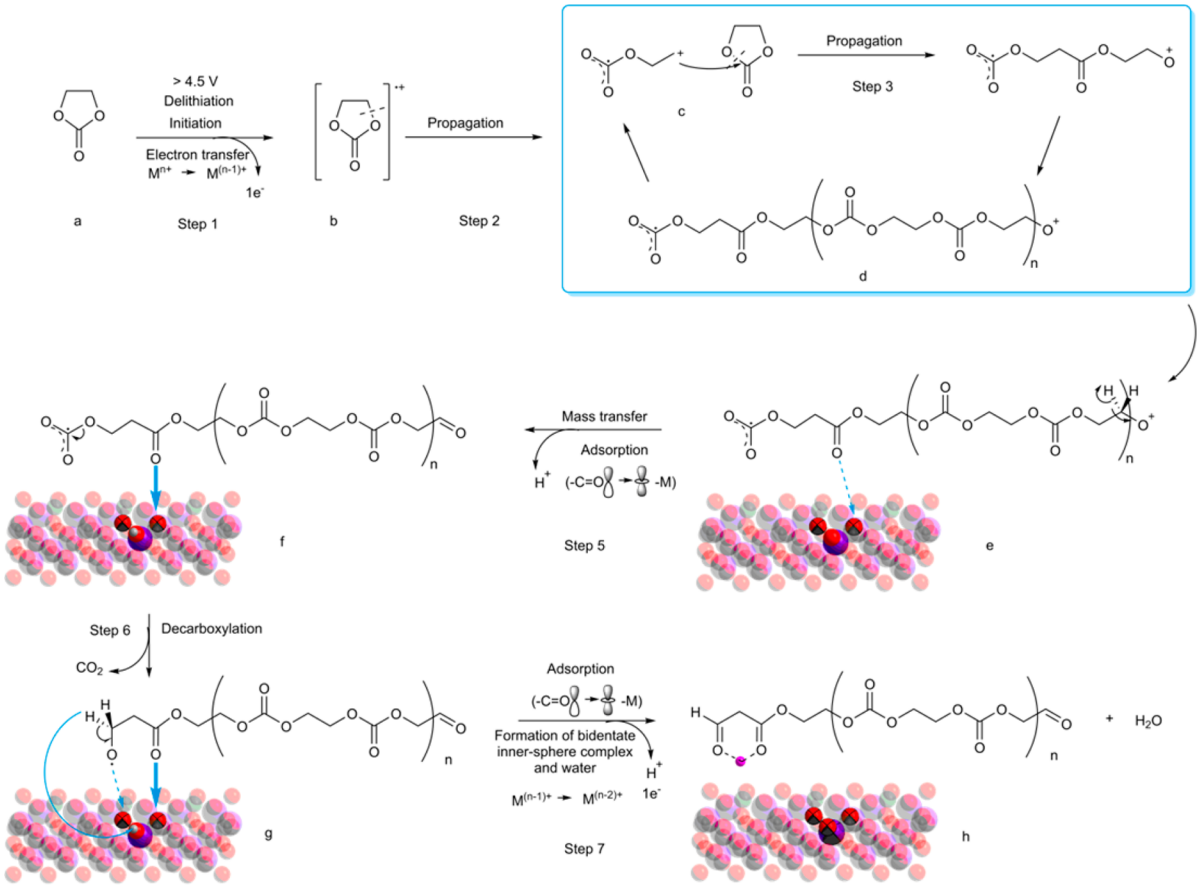

Figure 5. Possible formation pathway of the metal complexes upon oxidation of EC (a) at the $Li_xNi_{0.5}Mn_{1.5}O_4$ surface by propagation and PCET. Step 1: Initiation of the cation radical (b) at potentials >4.5 V leading to bond cleavage and EC ring opening. At this potential, an electron transfer induces a metal ion reduction $M^{n+}/M^{(n-1)+}$ in the structure ($Mn^{IV} \rightarrow Mn^{III}$ or preferentially $Ni^{IV} \rightarrow Ni^{III}$ for $E > 4.7$ V) . Steps 2 and 3: Propagation of the radical reaction leading to oligo(ether carbonate) cation radical formation (c–e). Step 5: Adsorption of radicals on the $Li_xNi_{0.5}Mn_{1.5}O_4$ surface accompanied by proton transfer (f). Step 6: Decarboxylation leading to generation of carbon dioxide (g). Step 7: PCET via attack on the C–H bond by OH surface species, leading to heterolytic C–H cleavage that results in metal ion reduction ($Mn^{III} \rightarrow Mn^{II}$ or preferentially $Ni^{III} \rightarrow Ni^{II}$ for $E >$ 4.7 V), desorption of water, and dissolution of metal in the electrolyte as a bidentate complex (h).

The first electron transfer from the nonbonding oxygen lone electron pair in the carbonyl group of the adsorbed DEC molecule to the surficial Mn^{IV} reduces the Mn^{IV} to Mn^{III} and yields a DEC cation radical adsorbed at the surface (Figure 4c). The C–H bond of the DEC cation radical is attacked by nucleophilic surface oxygen, which leads to heterolytic cleavage of hydrogen from the ethyl group, protonation of the adjacent unsaturated surface oxygen atoms in $Li_xNi_{0.5}Mn_{1.5}O_{4-\delta}$, and the formation of hydroxyl surface species (Figure 4c,d). This is also accompanied by C–O bond cleavage in the DEC cation radical and the formation of an acetaldehyde (Figure 4d).The second PCET process occurs when the C–H bond of the methyl group in the acetaldehyde reacts with the surface OH^- group. This heterolytic cleavage produces an acetaldehyde radical adsorbed to the surficial Mn^{III} via the nonbonding electron pairs of oxygen in the carbonyl group, as well as a water molecule (Figure 4e). In the following step, two adjacent adsorbed acetaldehyde radicals recombine to form a bidentate ligand adsorbed at the Mn^{III} site[44] (Figure 4f). The bidentate-ligand double bond significantly weakens the strength of the neighboring Mn–O bonds at the surface of the $Li_xNi_{0.5}Mn_{1.5}O_{4-\delta}$ lattice[45] and facilitates removal of the surficial Mn^{III} β-diketonate coordination complex (Figure 4g). This chain of reactions creates even more surface oxygen vacancies and coordination sites, which further catalyzes DEC oxidation and manganese dissolution. If no adjacent Mn^{IV} is available (Figure 4, step 4), the second electron transfer from a DEC radical occurs on a surficial Mn^{III} (Figure 4e), reducing it to Mn^{II}. This is followed by its dissolution in the form of a Mn^{II} β-diketonate coordination complex.

The oxidation of EC at $Li_xNi_{0.5}Mn_{1.5}O_{4-\delta}$ (Figure 5) involves a stepwise mechanism with two electron transfers and two proton transfers. At potentials above 4.5 V, oxidation of the physisorbed EC molecules is initiated by EC ring opening, formation of a cation radical (Figure 5b), and reduction of Mn^{IV} to Mn^{III} (Figure 5, step 1). The cation radical reacts with another EC molecule at the $Li_xNi_{0.5}Mn_{1.5}O_{4-\delta}$ surface (Figure 5, steps 2 and 3), yielding oligo(ether carbonate) polymer radicals, which can recombine to form high-molecular-weight oligo(ether carbonate) chains via the propagation mechanism (Figure 5d). The polymer propagation reaction and associated polymer chain growth can stop randomly by deprotonation of the cation radical and formation of OH^- surface species, similar to the mechanism proposed for DEC oxidation. The terminal carbonate group at the other end of this elongated polymer molecule undergoes decarboxylation followed by PCET from the adsorbed polymer radical to the Mn^{III} site, which, as in DEC oxidation, leads to the formation of water and Mn^{II}

DOI: 10.1021/ja5116698
J. Am. Chem. Soc. 2015, 137, 3533–3539

coordination complexes with β-diketonate chelate ligands in the first coordination shell. At potentials >4.7 V, Ni^{IV} sites in the vicinity of lithium, manganese, and oxygen vacancies become accessible, and the formation of Ni^{II} complexes analogous to the Mn^{II} species occurs. Oxidation of EC at these surficial Ni^{IV} site leads to Ni^{II} complexes with longer oligo(ether) side chains because of the lower number of adjacent oxygens, which are necessary to stop the chain growth by deprotonation. The long side chain decreases the solubility of the resultant Mn^{III}/Mn^{II} and Ni^{II} complexes, which explains the variety of the observed soluble and insoluble fluorescent compounds in aged/cycled Li-ion cells. The Ni^{II} β-diketonate complexes with longer alkoxide side chains from EC oxidation tend to precipitate and form surface films, whereas the more soluble $Mn^{II/III}$ β-diketonate complexes, which mostly originate from DEC, diffuse into the electrolyte and ultimately get incorporated into the SEI layer on the negative electrode. A decarboxylation reaction of EC is also common for the proposed mechanisms of formation of Mn oxalates and Ni carbonates at lithium Ni/Mn oxide-based electrodes.[2,4,46]

The possible effect of the Ni^{II} and $Mn^{II/III}$ β-diketonate coordination complexes on the Li^+ transport in the SEI layer and the overall degradation of electrochemical performance of the Li-ion cell are still unclear. The Mn dissolution and subsequent incorporation in the SEI layer on the negative electrode inhibits Li^+ transport and contributes to the observed $Li_xNi_{0.5}Mn_{1.5}O_{4-\delta}$/graphite cell impedance rise and capacity loss.[4,7] Interestingly, the proposed mechanism of $Li_xNi_{0.5}Mn_{1.5}O_{4-\delta}$ dissolution may apply for the whole class of lithiated transition-metal oxide materials for Li-ion positive electrodes that operate at potentials >4.2 V. The process of metal dissolution involves EC and/or DEC oxidation on transition-metal sites in the presence of surface defects (i.e., oxygen vacancies), which are quite common for these materials. This immediately implies that similar phenomena may occur in organic-carbonate-based electrolytes at the surface of other transition-metal oxides (e.g., $Li_xCoO_{2-\delta}$, $Li_xNiO_{2-\delta}$, $Li_xMn_2O_{4-\delta}$ and $Li_{1\pm x}NiyCozMn\beta O_{2-\delta}$). On the other hand, the results of this study may offer unique insight into the mechanism of Li^+ transport across the solid electrolyte interphases in Li-ion systems.

CONCLUSION

X-ray absorption and optical fluorescence spectroscopy and imaging experiments demonstrated that electrochemical oxidation of DEC and EC at the $Li_xNi_{0.5}Mn_{1.5}O_{4-\delta}$ electrode at potentials >4.2 V leads to the formation of fluorescent Ni^{II} and $Mn^{II/III}$ complexes with β-diketonate ligands and Ni^{II} and Mn^{II} oxalates and carbonates. Stepwise and all-concerted proton-coupled electron transfer reaction mechanisms that lead to the formation of metal complexes and water at the $Li_xNi_{0.5}Mn_{1.5}O_{4-\delta}$ surface are proposed and discussed. The rate of these reactions is enhanced by the continuous creation of oxygen vacancies. The adsorption of β-diketonate chelate ligands at Ni^{IV}/Mn^{IV} surface sites greatly facilitates Ni/Mn removal from the crystalline lattice and is primarily responsible for the observed Ni/Mn dissolution. The postulated heterogeneous catalysis mechanism accurately describes interfacial processes on the $Li_xNi_{0.5}Mn_{1.5}O_{4-\delta}$ positive electrode in organic carbonate electrolytes and relates to the observed failure modes in Li-ion batteries. On the other hand, this unique electrochemical process presents a new reaction pathway for possible electrosynthesis of optically active organic compounds.

ASSOCIATED CONTENT

Supporting Information

Detailed experimental procedures. This material is available free of charge via the Internet at http://pubs.acs.org.

AUTHOR INFORMATION

Corresponding Author

*r_kostecki@lbl.gov

Notes

The authors declare no competing financial interest.

ACKNOWLEDGMENTS

This work was supported by the Assistant Secretary for Energy Efficiency and Renewable Energy, Office of Vehicle Technologies, U.S. Department of Energy, under Contract DE-AC02-05CH11231. Y.-S.Y. was supported by the Northeastern Center for Chemical Energy Storage, an Energy Frontier Research Center funded by the U.S. Department of Energy, Office of Science, Office of Basic Energy Sciences under Award DE-SC0001294. Beamline 10.3.2 at the Advanced Light Source is supported by the Director, Office of Science, Office of Basic Energy Sciences, U.S. Department of Energy under Contract DE-AC02-05CH11231. The authors thank Dr. Matthew Marcus (LBNL) for his help with the XANES experiments and data analysis. The authors also gratefully acknowledge Dr. Vincent S. Battaglia and Dr. Yanbao Fu (LBNL) for fruitful discussions and for supplying electrode materials.

REFERENCES

(1) Ellis, B. L.; Lee, K. T.; Nazar, L. F. *Chem. Mater.* **2010**, *22*, 691−714.
(2) Goodenough, J. B.; Kim, Y. *Chem. Mater.* **2010**, *22*, 587−603.
(3) Moshkovich, M.; Cojocaru, M.; Gottlieb, H. E.; Aurbach, D. *J. Electroanal. Chem.* **2001**, *497*, 84−96.
(4) Sloop, S. E.; Kerr, J. B.; Kinoshita, K. *J. Power Sources* **2003**, *119*, 330−337.
(5) Armstrong, A. R.; Holzapfel, M.; Novák, P.; Johnson, C. S.; Kang, S.-H.; Thackeray, M. M.; Bruce, P. G. *J. Am. Chem. Soc.* **2006**, *128*, 8694−8698.
(6) Pieczonka, N. P. W.; Liu, Z.; Lu, P.; Olson, K. L.; Moote, J.; Powell, B. R.; Kim, J.-H. *J. Phys. Chem. C* **2013**, *117*, 15947−15957.
(7) Ammundsen, B.; Paulsen, J. *Adv. Mater.* **2001**, *13*, 943−956.
(8) Demeaux, J.; Lemordant, D.; Caillon-Caravanier, M.; Galiano, H.; Claude-Montigny, B. *Electrochim. Acta* **2013**, *89*, 163−172.
(9) Tarascon, J. M.; Armand, M. *Nature* **2001**, *414*, 359−367.
(10) Winter, M.; Besenhard, J. O.; Spahr, M. E.; Novák, P. *Adv. Mater.* **1998**, *10*, 725−763.
(11) Thackeray, M. M.; Johnson, P. J.; de Picciotto, L. A.; Bruce, P. G.; Goodenough, J. B. *Mater. Res. Bull.* **1984**, *19*, 179−187.
(12) Zhan, C.; Lu, J.; Kropf, A. J.; Wu, T.; Jansen, A. N.; Sun, Y.-K.; Qiu, X.; Amine, K. *Nat. Commun.* **2013**, *4*, No. 2437.
(13) Park, M.; Zhang, X.; Chung, M.; Less, G. B.; Sastry, A. M. *Chem. Mater.* **2014**, *26*, 3128−3134.
(14) Shkrob, I. A.; Kropf, A. J.; Marin, T. W.; Li, Y.; Poluektov, O. G.; Niklas, J.; Abraham, D. P. *J. Phys. Chem. C* **2014**, *118*, 24335−24348.
(15) Cabana, J.; Zheng, H.; Shukla, A. K.; Kim, C.; Battaglia, V. S.; Kunduraci, M. *J. Electrochem. Soc.* **2011**, *158*, A997−A1004.
(16) Hai, B.; Shukla, A. K.; Duncan, H.; Chen, G. *J. Mater. Chem. A* **2013**, *1*, 759−769.
(17) Cabana, J.; Zheng, H.; Shukla, A. K.; Kim, C.; Battaglia, V. S.; Kunduraci, M. *Chem. Mater.* **2012**, *24*, 2952−2964.
(18) Islam, M. S.; Fisher, C. A. J. *Chem. Soc. Rev.* **2014**, *43*, 185−204.
(19) Karim, A.; Fosse, S.; Persson, K. A. *Phys. Rev. B* **2013**, *87*, No. 075322.

DOI: 10.1021/ja5116698
J. Am. Chem. Soc. 2015, 137, 3533−3539

(20) Sushko, P. V.; Rosso, K. M.; Zhang, J.-G.; Liu, J.; Sushko, M. L. *Adv. Funct. Mater.* **2013**, *23*, 5530−5535.
(21) Xiao, J.; Chen, X. L.; Sushko, P. V.; Sushko, M. L.; Kovarik, L.; Feng, J. J.; Deng, Z. Q.; Zheng, J. M.; Graff, G. L.; Nie, Z. M.; Choi, D. W.; Liu, J.; Zhang, J. G.; Whittingham, M. S. *Adv. Mater.* **2012**, *24*, 2109−2116.
(22) Adler, S. B.; Chen, X. Y.; Wilson, J. R. *J. Catal.* **2007**, *245*, 91−109.
(23) Al-Abadleh, H. A.; Grassian, V. H. *Surf. Sci. Rep.* **2003**, *52*, 63−161.
(24) Verma, P.; Maire, P.; Novák, P. *Electrochim. Acta* **2010**, *55*, 6332−6341.
(25) Park, M.; Zhang, X.; Chung, M.; Less, G. B.; Sastry, A. M. *J. Power Sources* **2010**, *195*, 7904−7929.
(26) Costentin, C.; Robert, M.; Savéant, J.-M.; Tard, C. *Acc. Chem. Res.* **2014**, *47*, 271−280.
(27) Buurmans, I. L. C.; Weckhuysen, B. M. *Nat. Chem.* **2012**, *4*, 873−886.
(28) Kostecki, R.; Norin, L.; Song, X.; McLarnon, F. *J. Electrochem. Soc.* **2004**, *151*, A522−A526.
(29) Norberg, N. S.; Lux, S. F.; Kostecki, R. *Electrochem. Commun.* **2013**, *34*, 29−32.
(30) Baddour-Hadjean, R.; Pereira-Ramos, J. P. *AIP Conf. Proc.* **2010**, *1267*, 1137−1138.
(31) Choi, N.-S.; Chen, Z.; Freunberger, S. A.; Ji, X.; Sun, Y.-K.; Amine, K.; Yushin, G.; Nazar, L. F.; Cho, J.; Bruce, P. G. *Angew. Chem., Int. Ed.* **2012**, *51*, 9994−10024.
(32) Aziz, E. F.; Rittmann-Frank, M. H.; Lange, K. M.; Bonhommeau, S.; Chergui, M. *Nat. Chem.* **2010**, *2*, 853−857.
(33) Cordes, T.; Blum, S. A. *Nat. Chem.* **2013**, *5*, 993−999.
(34) Tseng, T.-C.; Urban, C.; Wang, Y.; Otero, R.; Tait, S. L.; Alcamí, M.; Écija, D.; Trelka, M.; Gallego, J. M.; Lin, N.; Konuma, M.; Starke, U.; Nefedov, A.; Langner, A.; Wöll, C.; Herranz, M. Á.; Martín, F.; Martín, N.; Kern, K.; Miranda, R. *Nat. Chem.* **2010**, *2*, 374−379.
(35) Nam, K.-W.; Bak, S.-M.; Hu, E.; Yu, X.; Zhou, Y.; Wang, X.; Wu, L.; Zhu, Y.; Chung, K.-Y.; Yang, X.-Q. *Adv. Funct. Mater.* **2013**, *23*, 1047−1063.
(36) Nishikawa, Y.; Nakamura, Y.; Kawaguchi, S. *Bull. Chem. Soc. Jpn.* **1972**, *45*, 155−160.
(37) Kryukov, A. I.; Tkachenko, Z. A.; Bukhtiyarov, V. K.; Kriss, E. E. *Theor. Exp. Chem.* **1983**, *19*, 176−182.
(38) Babich, I. V.; Plyuto, Y. V.; Van Langeveld, A. D.; Moulijn, J. A. *Appl. Surf. Sci.* **1997**, *115*, 267−272.
(39) Bullen, G. J.; Mason, R.; Pauling, P. *Inorg. Chem.* **1965**, *74*, 456−462.
(40) Vovna, V. I.; Korochentsev, V. V.; Komissarov, A. A.; L'vov, I. B. *Russ. J. Phys. Chem. B* **2013**, *7*, 220−224.
(41) Borodin, O.; Jow, T. R. *ECS Trans.* **2011**, *33*, 77−84.
(42) Kumar, N.; Leung, K.; Siegel, D. J. *J. Electrochem. Soc.* **2014**, *161*, E3059−E3065.
(43) Duckworth, O. W.; Martin, S. T. *Geochim. Cosmochim. Acta* **2001**, *65*, 4289−4301.
(44) Costentin, C.; Robert, M.; Savéant, J.-M.; Teillout, A.-L. *Proc. Natl. Acad. Sci. U.S.A.* **2009**, *106*, 11829−11836.
(45) Schäfer, H. J. *Angew. Chem., Int. Ed. Engl.* **1981**, *20*, 911−934.
(46) Jun, Y.-S.; Martin, S. T. *Environ. Sci. Technol.* **2003**, *37*, 2363−2370.
(47) Li, S. R.; Chen, C. H.; Xia, X.; Dahn, J. R. *J. Electrochem. Soc.* **2013**, *160*, A1524−A1528.

DOI: 10.1021/ja5116698
J. Am. Chem. Soc. 2015, 137, 3533−3539